

ANALYSIS OF ASTEROID (216) KLEOPATRA USING DYNAMICAL AND STRUCTURAL CONSTRAINTS

MASATOSHI HIRABAYASHI¹ AND DANIEL J. SCHEERES²

¹ Aerospace Engineering Sciences, 429 UCB, University of Colorado, Boulder, CO 80309-5004, USA; masatoshi.hirabayashi@colorado.edu

² Aerospace Engineering Sciences, 429 UCB, University of Colorado, Boulder, CO 80309-0429, USA

Received 2013 April 12; accepted 2013 November 4; published 2013 December 20

ABSTRACT

This paper evaluates a dynamically and structurally stable size for Asteroid (216) Kleopatra. In particular, we investigate two different failure modes: material shedding from the surface and structural failure of the internal body. We construct zero-velocity curves in the vicinity of this asteroid to determine surface shedding, while we utilize a limit analysis to calculate the lower and upper bounds of structural failure under the zero-cohesion assumption. Surface shedding does not occur at the current spin period (5.385 hr) and cannot directly initiate the formation of the satellites. On the other hand, this body may be close to structural failure; in particular, the neck may be situated near a plastic state. In addition, the neck's sensitivity to structural failure changes as the body size varies. We conclude that plastic deformation has probably occurred around the neck part in the past. If the true size of this body is established through additional measurements, this method will provide strong constraints on the current friction angle for the body.

Key words: celestial mechanics – comets: general – methods: analytical – methods: numerical – minor planets, asteroids: general – minor planets, asteroids: individual (216 Kleopatra)

Online-only material: color figures

1. INTRODUCTION

Asteroid (216) Kleopatra, classified as an M-type in the Tholen (1984) taxonomy or as a Xe-type in the Bus & Binzel (2002) taxonomy, has been of interest for a few decades due to its odd shape and fast spin rate. It orbits in the main belt, and asteroids of this type have not been targeted yet; therefore, this asteroid is not well understood.

1.1. Observational Studies for Asteroid (216) Kleopatra

We have significant information on (216) Kleopatra including the shape (Ostro et al. 2000), the spin period (5.385 hr, Magnusson 1990), and the mass (4.64×10^{18} kg, Descamps et al. 2011). Not as certain, and subject to different interpretations, is its total size.

Past studies have investigated this asteroid's shape by different observation techniques. From light-curve observations, Scaltriti & Zappala (1978) confirmed shape elongation of this asteroid and small differences of the magnitudes at the maxima and the minima (see Figure 4 in their paper). They pointed out that those differences came from either different reflectivity or a shadowing effect. Weidenschilling (1980) estimated (624) Hektor as a binary asteroid whose components are nearly in contact, considering a hydrostatically stable equilibrium shape. Then, he applied this technique to (216) Kleopatra, which has a (624) Hektor-like light curve, and showed that an amplitude of 3.3 mags slightly exceeds the value of a contact binary, but a contact binary model with its spin period recovers a reasonable density of 3.9 g cm^{-3} . Light-curve observations by Zappala et al. (1983) revealed that a triaxial ellipsoid model fits their observations. On the other hand, Cellino et al. (1985) found that a binary model is compatible with their light-curve data. They also pointed out that the amplitude of 0.9 mag by Zappala et al. (1983) is an estimation, while the amplitude of this asteroid highly depends on the phase. Occultations by Dunham et al. (1991) estimated the size as dimensions of 230 km by 55 km. Furthermore, Mitchell et al. (1995) performed radar observations; however, although they obtained Kleopatra echoes which

are similar to those of bifurcated asteroid (4769) Castalia, their coarse data set precluded them from determining the shape. They also attempted to detect the shape from occultation data; however, since the model used was simplistic, they could obtain no evidence for a bifurcation.

From comprehensive radar observations, Ostro et al. (2000) constructed a three-dimensional bi-lobed polyhedral shape model with dimensions of 217 km by 94 km by 81 km, although they indicated that the absolute size uncertainty was up to 25%. On the other hand, from the Fine Guidance Sensors (FGS) aboard the *Hubble Space Telescope (HST)*, Tanga et al. (2001) confirmed that their shape model is consistent with radar observations by Ostro et al. (2000).

Later studies compared their observation analyses with the Ostro et al. (2000) model. Hestroffer et al. (2002a) showed that a larger and more elongated model is consistent with the occultations as well as the photometric and interferometric *HST/FGS* results. Adaptive-optics observations by Hestroffer et al. (2002b) showed that their model is consistent with the Ostro et al. (2000) shape model, although these observations could not rule out the possibility that this asteroid is a binary asteroid. Takahashi et al. (2004) performed light-curve simulations based on the binary model by Cellino et al. (1985), the contact binary model by Tanga et al. (2001), and the polyhedron model by Ostro et al. (2000) to report that while the binary model and the contact binary model fit their light-curve simulations, the Ostro et al. (2000) shape model could not. It is worth noting that for simulations using the Ostro et al. (2000) shape model, they used the size estimated by Ostro et al. (2000), which may be smaller than the actual size.

From near-infrared adaptive-optics observations, Descamps et al. (2011) calculated the mass as 4.64×10^{18} kg from the mutual gravitational interaction between (216) Kleopatra and its satellites. Kaasalainen & Viikinkoski (2012) attempted to construct a new shape model, using multiple observational data (photometry, adaptive optics, occultation timings, and interferometry); however, they mentioned that the data were

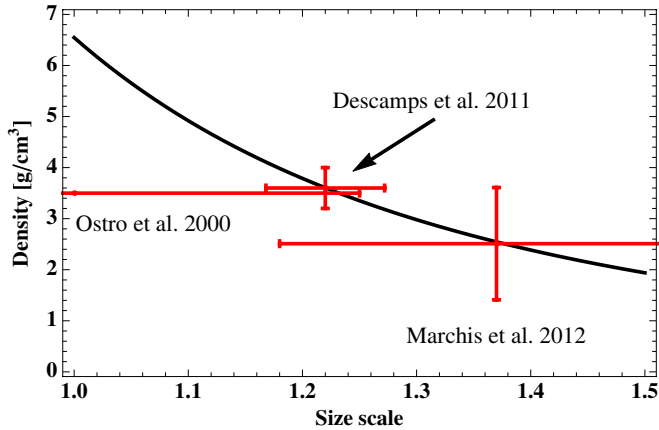


Figure 1. Relation between the size scale and the density. Given the mass of 4.64×10^{18} kg by Descamps et al. (2011) and the shape by Ostro et al. (2000), the curve describes the ideal density as a function of the size scale. The actual density and the size scale should be on this curve. The error bars are observation values by Ostro et al. (2000), Descamps et al. (2011), and Marchis et al. (2012). Note that Marchis et al. (2012) did not take into account the shape modification for their estimation (F. Marchis 2013, private communication).

(A color version of this figure is available in the online journal.)

not compatible and thus further analyses are necessary. We look forward to their new shape model.

Ostro et al. (2000) estimated the equivalent diameter³ as 108.6 km by radar observations and the surface bulk density as 3.5 g cm^{-3} from the surface reflectivity. Note that the latest version of the shape model provides a mass of $7.09 \times 10^5 \text{ km}^3$, which is equal to an equivalent diameter of 111.1 km. Tedesco et al. (2002) reported the *IRAS* equivalent diameter as 135.07 km, while the estimation by Descamps et al. (2011) is consistent with the Tedesco et al. (2002) size. On the other hand, from observations with *Spitzer*/IRS, Marchis et al. (2012) derived the equivalent diameter as 152.5 km by using the Near-Earth Asteroid Thermal Model (we referred to Table 5 in their paper). These papers indicate that the size of (216) Kleopatra is not well understood. Figure 1 shows the comparison between the estimated size scale and the bulk density. Scale size means an equivalent diameter relative to that of the Ostro et al. (2000) size, i.e., $7.09 \times 10^5 \text{ km}^3$. The Ostro et al. (2000) size is 1.00, the Descamps et al. (2011) size is 1.22, and the Marchis et al. (2012) size is 1.37. For Ostro et al.’s (2000) estimation, we only show the error bar of the size scale (the region of the horizontal axis). Note that the Ostro et al. (2000) density is based on their surface reflectivity estimation.

From these papers, it seems that the Ostro et al. (2000) shape has been confirmed by other teams but that the size has not. This study, therefore, utilizes the Ostro et al. (2000) shape and keeps its size as a free parameter. Note that although our model provides insight on a surprisingly important role that the total size is related to its stability, future measurements will be able to provide real insight on the strength of this body by using our current analysis.

1.2. Theoretical Studies of the Internal Structure of a Rotating Ellipsoid

Theoretical studies of the internal structure of a rotating triaxial ellipsoid have been of interest for a long time. In particular, the elastic stresses have been discussed for more than

100 years. Chree (1889) provided a complete elastic solution for a rotating sphere in terms of polar coordinates, although Chree (1891) pointed out that an application of the Chree (1889) theory to the Earth may be limited because the dependency of the initial internal stress state on the history causes difficulty in determining the ellipticity. Love (1944) discussed this point in detail⁴ and avoided this difficulty by assuming that a rotating body is homogeneous and incompressible. Dobrovolskis (1982) provided an elastic solution in Cartesian coordinates with a nearly incompressible Poisson’s ratio of $\nu = 0.46$, but gave the comment that this Poisson’s ratio eases the difficulty for the sudden collapse of the surface due to turning on the self-gravity; this situation may be unrealistic. Washabaugh & Scheeres (2002) focused on the elastic energy of a rotating ellipsoid; they found that the stress state in the compressible case can relax around the lowest elastic energy point more easily than that in the incompressible case. Kadish et al. (2008), on the other hand, investigated internal elastic stresses of a uniformly rotating self-gravitating accreted ellipsoid.

On the contrary, approaches using plastic theory are relatively new. Deriving a general solution of the internal stress on the zero-cohesion assumption with regard to the Mohr–Coulomb (MC) yield criterion, Holsapple (2001) found that for a uniformly rotating ellipsoid, the upper-limit load and the lower-limit load are identical. Holsapple (2004) proposed new definitions of local stability of shapes and applied this stability condition to a uniformly rotating solid ellipsoid. On the other hand, in the case of a rod, a disk, and an ellipsoid, Holsapple (2008) confirmed that an actual failure occurs between the lower- and upper-limit loads. Holsapple (2010) derived deformation paths of an ellipsoid due to a YORP-induced spin. His result was consistent with numerical simulations by Sanchez & Scheeres (2012). Using a plastic material condition with regard to the Drucker-Prager yield criterion, Sharma (2010) formulated equilibrium shapes of rubble-pile binaries and investigated the current material properties of contact binary asteroids. In this experiment, he modeled (216) Kleopatra as a contact binary and mentioned, “We will model Kleopatra as a congruent contact binary with prolate ellipsoidal members. We thus ignore the “bridge” connecting the binary’s members, thereby assuming that the bridge’s internal strength and mass are negligible.”

1.3. Outline of the Present Study

Our goal here is to investigate the failure mode that (216) Kleopatra most likely experiences and to evaluate a structurally stable size in the hope of finding constraints on and predictions of what its current size should be. The spin rate by Magnusson (1990), the shape model by Ostro et al. (2000), and the mass by Descamps et al. (2011) are considered to be constant properties, while the size is varied for determining the stable size. This paper discusses two possible failure modes: material shedding from the surface and structural failure due to plastic deformation.

The surface-shedding condition is given by using zero-velocity curves. This technique allows us to visualize allowable and non-allowable regions of orbital motion of a massless particle about the primary and its dynamical equilibrium points. It is also interesting that surface shedding initiates the formation of the satellites. According to Descamps et al. (2011), the satellites are formed by material shedding. We develop a model used for predicting whether or not these satellites result from surface shedding.

³ An equivalent diameter is a diameter of a sphere with the same volume as the shape.

⁴ See Articles 75 and 176 in Love (1944).

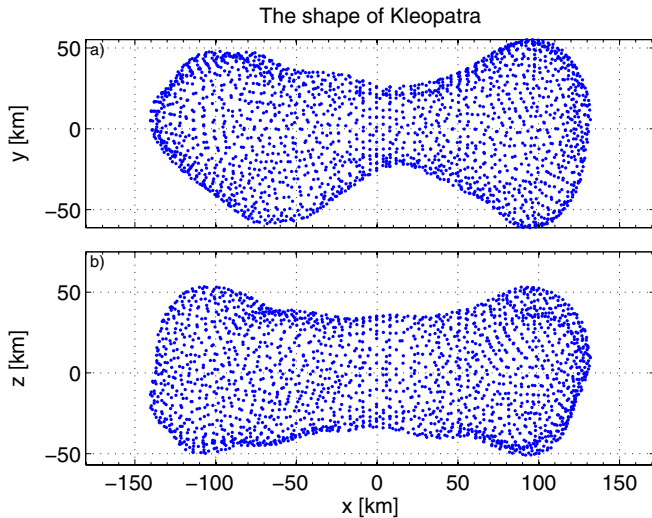


Figure 2. Projection of (216) Kleopatra’s shape model by Ostro et al. (2000). This shape model consists of surface points (vertices) and the order of surface elements (faces). The plot shows the vertices in a Cartesian coordinate frame. The upper plot shows the projection onto the $x-y$ plane, while the lower plot is onto the $x-z$ plane. Note that x , y , and z lie along the minor, intermediate, and major principal axis, respectively. The size scale of these plots is adjusted so as to be the same as 1.22, i.e., the Descamps et al. (2011) size. (A color version of this figure is available in the online journal.)

On the other hand, the structural-failure condition is discussed by a limit analysis. Note that a limit analysis explicitly assumes that materials are elastic-perfectly plastic, the yield envelope is smoothly convex, the material behavior follows an associated flow rule, and the velocity fields are homogeneous. This technique gives the lower and upper bounds of structural failure. The lower bound is the condition where a body does not experience plastic collapse. We obtain this bound by solving elastic solutions with commercial finite element software ANSYS (Academic Teaching Introductory, 14.0). On the other hand, the upper bound is the condition where a body must fail plastically due to its limit load. We calculate this bound for both a whole volume and a partial volume. To determine plastic failure of a partial volume, we assume that (216) Kleopatra is symmetric about the principal axes.

This paper is organized as follows: The first part summarizes physical properties used in this analysis. The second part defines surface shedding and structural failure. Third, this paper introduces the techniques for determining these failure modes. Then, the surface-shedding condition and the failure condition are compared. In particular, the satellites’ formation and the stable-size estimation are the prime results in this paper.

2. KNOWN PHYSICAL PARAMETERS OF ASTEROID (216) KLEOPATRA

The spin period is fixed at 5.385 hr (Magnusson 1990). On the other hand, we utilize the shape model by Ostro et al. (2000) available at <http://echo.jpl.nasa.gov/>. Figure 2 shows the projection of the surface points onto the $x-y$ and $x-z$ plane, where x , y , and z are the minor principal axis, the intermediate principal axis, and the major principal axis, respectively. The size in this figure is the same as the estimation by Descamps et al. (2011). The bifurcation structure can be confirmed in the middle of the body. Furthermore, the mass is fixed at the Descamps et al. (2011) mass, i.e., 4.64×10^{18} kg. Those properties are described in Table 1. This analysis assumes density

Table 1
Constant Properties of (216) Kleopatra

Property	Value	Units	Reference
Mass	4.64×10^{18}	kg	Descamps et al. (2011)
Period	5.385	hr	Magnusson (1990)
Cohesion	0	N m^{-3}	Holsapple (2007)
Shape	Ostro et al. (2000)

Table 2
Physical Properties of (216) Kleopatra’s Satellites

Property	Satellite (Outer)	Satellite (Inner)
Diameter (km)	8.9 ± 1.6	6.9 ± 1.6
Orbital period (days)	2.32 ± 0.02	1.24 ± 0.02
Semi-major axis (km)	678 ± 13	454 ± 6
Orbit pole right ascension (deg)	74 ± 2	79 ± 2
Orbit pole declination (deg)	16 ± 1	16 ± 1

Note. Note that the primary’s spin pole is given by $\lambda = 76^\circ \pm 3^\circ$ and $\beta = 16^\circ \pm 1^\circ$ in J2000 ecliptic coordinates (Descamps et al. 2011).

homogeneity and uniform rotation. In addition, physical parameters of the satellites are given by Descamps et al. (2011) (see Table 2). To discuss dynamics of the satellites, we assume that the orbital planes of the satellites are parallel to the equatorial plane of (216) Kleopatra. This result comes from the hypothesis of Descamps et al. (2011); however, it finally allowed them to derive a relevant orbit solution. Moreover, from the observation of a stellar occultation by (216) Kleopatra in 1980 (see Section 3.4 in Descamps et al. 2011), they could interpret the reported secondary event from their simple solution (P. Descamps 2013, private communication).

Material properties are also critical parameters for characterizing the body behavior, although they are usually unknown. It is assumed that materials considered here are elastic-perfectly plastic, the yield envelope is smoothly convex, the material behavior follows an associated flow rule, and the velocity fields are homogeneous. Those assumptions are crucial in using a limit analysis. Here, the MC yield criterion, a function of a friction angle and cohesion, is utilized to describe (216) Kleopatra’s yield condition. This study assumes zero-cohesion. Holsapple (2007) reported that large bodies such as (216) Kleopatra are located in the gravity regime in which cohesion is negligible.

3. POSSIBLE FAILURE MODES

3.1. Surface Shedding

Surface shedding is a dynamical-oriented process of small particles on the surface. The process occurs due to the balance of the total forces acting on these particles. When the spin rate is above this condition, any particles that experience outward forces fly off and do not immediately come back to the surface (see the right side in Figure 3). At this point, the internal body should be below structural failure. Note that the necessary condition for loose material to fly off the surface is that *dynamical equilibrium points reach the surface*. Guibout & Scheeres (2003) gave a similar analysis for the surface stability of a uniformly spinning ellipsoid. Their results showed that as the spin period increases gradually, the stable regions move to the extremities along the minor principal axis. Finally, the saddle equilibrium points touch the surface and the stable regions disappear from the extremities. Throughout the text, we call this condition the “first shedding.”

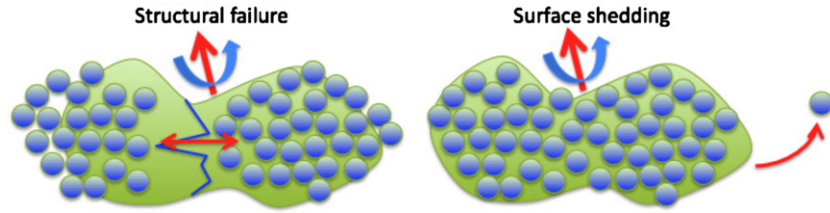


Figure 3. Structural failure (left) and surface shedding (right).
(A color version of this figure is available in the online journal.)

Another curious question is the origin of the satellites. Descamps et al. (2011) estimated the physical properties of the satellites (Table 2). They also stated, “as to the origin of Kleopatra’s companions, they could be a by-product of the spinning-up process leading to mass shedding in orbit.” Is it possible that surface materials were shed to form the satellites in the past? To answer this question, we perform a simple analysis, using the necessary condition of the first shedding.

3.2. Structural Failure

We define the term “structural failure” as the end condition where plastic flow spreads over a target volume given by arbitrary cuts. The volume experiencing structural failure subsequently deforms after the first yield. This statement implies that plastic flow appearing in a small volume does not always lead to structural failure. In such a case, when this element is unloaded, it is sustained by residual stress (Chakrabarty 2006). The present study focuses on structural failure of a slice perpendicular to the minor principal axis, because the centrifugal force causes the strongest tension and shear over this volume. At the structural-failure condition, the slice initiates a catastrophic breakup of a body, which is depicted on the left side in Figure 3. Note that the situation where a body is separated into two components may need further angular momentum gain from structural failure.

3.3. Relation between Surface Shedding and Structural Failure

Past investigations reported that surface shedding and structural failure are highly correlated in terms of shapes and material properties. Eriguchi et al. (1982) pointed out that a symmetrically incompressible fluid becomes a dumbbell shape before a breakup, while an asymmetrically incompressible fluid becomes pear-shaped before mass shedding. Using the N -body code, pkdgrav, Walsh et al. (2008) and Walsh et al. (2012) demonstrated that mass shedding from a spherical aggregate initiates a binary system. Their analysis also revealed that the (66391) 1999 KW4 type equatorial ridge may be formed by landslides. On the other hand, using a Soft-Sphere Discrete Element Code, Sanchez & Scheeres (2012) reported that particle-particle surface friction makes a spherical shape experience surface shedding near its equatorial plane and makes an ellipsoidal shape break into two components.

4. ANALYSIS METHOD

4.1. Determination of the First Shedding

We note that a classic technique of this type is to compute the effective gravity slope, which is the direction of the total force (usually the gravitational acceleration and the centrifugal acceleration) from the local downward normal. For example, Ostro et al. (2006) visualized the effective gravity slope of (66391) 1999 KW4. This technique is useful when one wants to

focus on the surface condition of general shapes. However, the capability of this technique is limited if one wants to track the orbital motion in the vicinity of the primary.

The zero-velocity curves allow us to visualize both the equilibrium points and the constraints on the motion. However, for the use of this method, there are some cautions that should be noted.

First, this computation only considers the balance between the gravitational acceleration and the centrifugal acceleration. In other words, some attractive and repulsive forces that may be significant in an asteroid’s environment are not involved in this analysis. For example, a cohesive force is one of the effective attractions that may be significant for a small asteroids. On the contrary, (216) Kleopatra is assumed to be zero-cohesion, so the zero-velocity curve computation gives reasonable estimations for the first shedding. Second, even when the spin state is below the first shedding, there is a phenomenon that ejects materials into space by some processes, i.e., saltation by landslides. The present technique does not consider this phenomenon. As given earlier, surface shedding is the process where any particles experiencing zero-forces are about to fly off and do not immediately come back to the surface after lifting off. This condition is different from the condition where particles are simply ejected from the surface. Particles ejected below the first shedding usually come back to the surface immediately and do not contribute to major collapse processes. Third, we assume that the original shape does not change. This assumption implicitly makes the first condition more conservative than the actual first shedding because shape deformation allows the equilibrium points to touch the surface at a slower spin period. Consideration of this effect is beyond the present paper.

4.1.1. Zero-velocity Curves

The motion of a massless particle affected by the gravity from the primary in the rotating frame is described as

$$\begin{aligned}\ddot{x} - 2\omega\dot{y} &= -U_x + \omega^2x, \\ \ddot{y} + 2\omega\dot{x} &= -U_y + \omega^2y, \\ \ddot{z} &= -U_z,\end{aligned}\quad (1)$$

where U is the potential and the subscripts of U mean the partial derivative with respect to the position. The x axis, the y axis, and the z axis lie along the minor principal axis, the intermediate principal axis, and the major principal axis, respectively.

The Jacobi integral C_J is given by multiplying each equation of Equation (1) by \dot{x} , \dot{y} , and \dot{z} , summing these equations, and integrating:

$$C_J = \omega^2(x^2 + y^2) - 2U - \dot{x}^2 - \dot{y}^2 - \dot{z}^2. \quad (2)$$

If $\dot{x} = \dot{y} = \dot{z} = 0$, then Equation (2) becomes

$$C_J \leq \omega^2(x^2 + y^2) - 2U. \quad (3)$$

Equation (3) gives constraints on the motion of the particle. The closed boundary defined by $C_J = \omega^2(x^2 + y^2) - 2U$ is the zero-velocity curve. It also describes the force that points normal to them and toward the allowable regions. In general cases, there exist more than four equilibrium points, especially when the primary is nearly spherical. However, because of its highly bifurcated shape, (216) Kleopatra only has four equilibrium points: two of them sitting along the minor principal axis (saddle points) and the other two lying around the intermediate principal axis (center points). When one of the equilibrium points first touches the surface,⁵ the condition is called the first shedding condition.

Yu & Baoyin (2012, 2013) investigated the zero velocity curves and the equilibrium points of (216) Kleopatra using the same technique that we showed above. We emphasize that our computation results are different from their results for the following reason: This paper uses a constant mass of 4.64×10^{18} kg based on comprehensive observations by Descamps et al. (2011). On the other hand, although Yu & Baoyin (2012, 2013) stated that Descamps et al. (2011) obtained an accurate mass, they utilized the estimations by Ostro et al. (2000), i.e., a volume of 7.09×10^5 km³ and a density of 3.6 g cm⁻³. In the Appendix, we describe a computational comparison between Yu & Baoyin (2012, 2013) and our calculation.

4.1.2. Numerical Search for the First Shedding

The numerical algorithm by Werner & Scheeres (1997) will be used to calculate accurate external gravity forces of a polyhedral model. The following is the numerical scheme: First, given a spin period, we compute the zero-velocity curves. Second, we explicitly calculate the equilibrium points in each iteration. If the zero-velocity curve at the energy level of the saddle points touches the surface, the iterative scheme stops; otherwise, the spin period is updated to be faster. At the same energy level, the saddle points usually reach the surface first. Since the size is a free parameter, our code searches for this spin period in the test size scale range (we will show the range later).

4.2. Determination of the Upper and Lower Bounds of Structural Failure

4.2.1. The Mohr–Coloumb Yield Criterion for Cohesionless Materials

The MC yield criterion for cohesionless materials is given as

$$g(\sigma_1, \sigma_3, \phi) \leq 0, \quad (4)$$

where

$$g(\sigma_1, \sigma_3, \phi) = \frac{\sigma_1 - \sigma_3}{2} \sec \phi + \frac{\sigma_1 + \sigma_3}{2} \tan \phi \quad (5)$$

and ϕ is the angle of internal friction. The principal stresses are denoted by σ_i ($i = 1, 2, 3$), where $\sigma_3 < \sigma_2 < \sigma_1$. The MC envelope is identical to the slopes touching the Mohr circle centered at $(\sigma_1 + \sigma_3)/2$ with a radius of $(\sigma_1 - \sigma_3)/2$ (see Figure 4) in the σ - τ space, where σ is the normal stress and τ is the shear stress. The slopes go through the origin, if materials are zero-cohesion. The angle between the slope and the σ axis is identical to ϕ . The elastic region is inside the yield envelope, while the plastic region is on the envelope.⁶

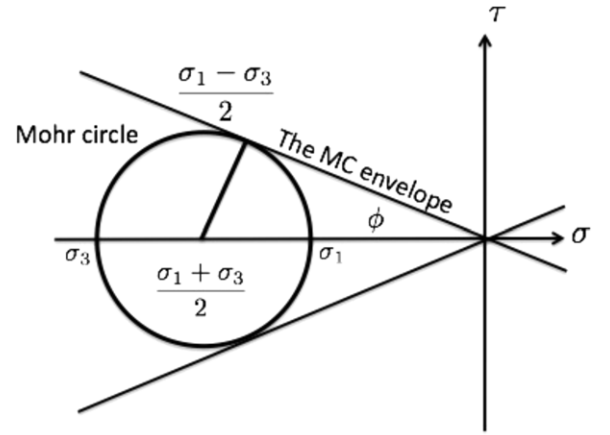


Figure 4. Mohr–Coloumb yield envelope identical to the slope touching a Mohr circle. The inclination depends on a material’s properties. If the stress state is within the envelope, only elastic deformation occurs. On the other hand, if the stress is on the envelope, a body experiences plastic strain.

In the three-dimensional principal stress space, the MC yield envelope is a hexagonal cone opening to the negative direction along the hydrostatic pressure and is not smooth at the tension and compression meridians. The smoothness of the yield envelope plays a role in a limit analysis technique. However, since our interest is to investigate real shapes, we barely encounter the stress state at these meridians.

4.2.2. Computation of Body Forces

The gravitational acceleration and the centrifugal acceleration are calculated by decomposing the original body into smaller elements: cubes (inside of the body) and polygons (on the surface). On the assumption that the density is constant and each element is so small that we can use a simple inverse-square law for spheres, the gravitational acceleration of element s is described as

$$\mathbf{b}_{sg} = -G\rho \sum_{t \neq s} \frac{V_t}{r_{st}^3} (\mathbf{r}_s - \mathbf{r}_t), \quad (6)$$

where ρ is the density, G is the gravitational constant, V is the volume of an element, and element t does not overlap s . \mathbf{r} is a position vector from the origin to an element and r is the Euclidean norm of \mathbf{r} . The centrifugal acceleration is described as

$$\mathbf{b}_{sc} = -\boldsymbol{\Omega} \times \boldsymbol{\Omega} \times \mathbf{r}_s = \Omega^2 \begin{bmatrix} x_s \\ y_s \\ 0 \end{bmatrix}, \quad (7)$$

where $\boldsymbol{\Omega}$ is the spin vector $\Omega[0, 0, 1]^T$. The total body force vector is now given as

$$\mathbf{b}_s = \mathbf{b}_{sg} + \mathbf{b}_{sc}. \quad (8)$$

The following discussion will use scalar notations b_i ($i = 1, 2, 3$) for the components of the body force vector, instead of vector notation \mathbf{b}_s . For computation of the stresses, b_i is substituted into the equilibrium equation, which is given as

$$\frac{\partial T_{ij}}{\partial x_j} + \rho b_i = 0, \quad (9)$$

where T_{ij} is a stress component in Cartesian coordinates.

⁵ The saddle point always reaches the surface first.

⁶ This comes from our assumption of elastic-perfectly plastic materials.

4.2.3. Limit Analysis

Limit analysis is a technique for calculating the plastic collapse load at which an idealized body deforms without limit. Here, an idealized body means that a body is characterized by (1) elastic-perfectly plastic materials, (2) convex yield criterion, (3) an associated flow rule, and (4) homogenous velocity fields. The last idealization allows us to apply average-stress techniques (shown below) to a determination of the upper bounds by a limit analysis. Further details of limit analysis can be found in Chen & Han (1988) and Chakrabarty (2006).

Let us discuss the definition and computation of the lower bound. According to Chen & Han (1988), the lower-bound theorem states, “if an equilibrium distribution of elastic stress can be found which balances the body force in a specific volume and the applied loads on the stress boundary and is everywhere below yield, then the body at the loads will not collapse.” This theorem is interpreted as the condition where there first appears an element at which the elastic stress reaches the yield. We solve an elastic solution on commercial finite element software ANSYS (Academic Teaching Introductory, 14.0). Then, we find a friction angle such that a stress state first appears on the yield envelope, i.e., $g(\sigma_1, \sigma_3, \phi) = 0$. This friction angle is always larger than the actual structural failure.

On the other hand, the upper-bound theorem states, “if plastic deformation is assumed to be zero on the displacement boundary, then the loads determined by equating the rate at which the external forces do work to the rate of internal dissipation will be either higher than or equal to the actual limit load.” We utilize the theorem by Holsapple (2008) that guarantees the equivalence of the upper-bound theorem and the yield condition of volume-average stresses. This paper uses two different types of volume-average stresses: the total-volume stress and the partial-volume stress. The total-volume stress is the stress averaged over the whole body, which provides global failure of the body:

$$\bar{T}_{ij}^t = \frac{1}{V} \int_V T_{ij} dv = \frac{1}{V} \int_V \rho x_j b_i dv, \quad (10)$$

where $i, j = 1, 2, 3$; $(x_1, x_2, x_3) = (x, y, z)$; and V describes the whole volume. This stress was also discussed by Holsapple (2008). For a real shape, however, the upper condition of this average stress is usually far away from the actual condition. For example, the stress state of a bifurcated body may be more complex than that of a spherical body. The partial-volume stress, which is newly defined in this paper, is the stress averaged over an arbitrary slice normal to the minor principal axis (see Figure 5):

$$\bar{T}_{ij}^p = \frac{1}{V_p} \int_{V_p} \rho x_j b_i dv + \frac{1}{V_p} \int_{S_p} l x_j T_{1i} dx_2 dx_3, \quad (11)$$

where l is the direction cosine of the external normal to the cross section perpendicular to the x axis; $l = 1$ for the cross section opening to the positive direction while $l = -1$ for that opening to the negative direction. The first term is an integral over the slice volume, V_p , while the second term is an integral over the cross sections, S_p . The upper-bound condition by this stress is closer to the actual structural failure if a slice is properly chosen.

Computation of Equation (10) and the first term of Equation (11) is straightforward; however, that of the second term of Equation (11) needs to be explained. If $j = 1$, then x_j can be treated as a constant value, and the integration becomes

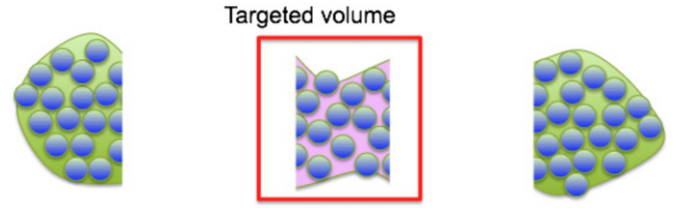


Figure 5. Illustration of the upper bound computation associated with the partial volume stress. To investigate structural failure of the neck, we consider the slice in the middle normal to the minor axis.

(A color version of this figure is available in the online journal.)

force balance on the cross sections. This procedure allows us to fix three out of six stress components. Computational difficulty of this term appears when $j \neq 1$. This results from the stress distribution on the cross sections. To avoid this difficulty, we assume that those three components are zero, using the fact that (216) Kleopatra is almost symmetric about the principal axes. After giving all stress components, we calculate the eigenvalues of this stress tensor to obtain the principal stresses.

The partial-volume stress will be used after the most sensitive slice to structural failure is determined. We search for the slice, considering a peak of the minimal principal axis component of normal stresses averaged over a cross section. The component is denoted as \bar{T}_{11}^a . Davidsson (2001) proposed this stress-average component to determine the failure condition of a biaxial body. Note that the area-stress technique will be used only for finding the location of the most sensitive cross section, but not for determining structural failure. Sharma (2009) reported that \bar{T}_{11}^a is identical to the yield condition of the averaged normal stresses with $\phi = 90^\circ$.

5. RESULTS

In this section, we show the results given in the range of the size scale from 1.0 to 1.5. In the following section, we call this range the test scale range.

5.1. Surface Shedding

5.1.1. First Shedding Condition

As an example, we show the first shedding condition of (216) Kleopatra with a size of 1.22. Figure 6(a) shows the zero-velocity curves at the current spin period, while Figure 6(b) is for the first shedding (2.85 hr). The red dots describe the shape projection onto the equatorial plane. The contour curves indicate the same energy levels, while the stars are the equilibrium points: two saddle points along the minor axis and two center points along the intermediate axis. In Figure 6(a), a massless particle on the surface is in the primary’s gravity-dominant region and cannot lift off because none of the equilibrium points touches the surface. However, as this asteroid spins faster, the equilibrium points move to the surface, and the gravity-dominant region shrinks. Eventually, as seen in Figure 6(b), the saddle point on the left side reaches the surface at 2.85 hr. In addition, the saddle point on the right side is also about to touch the surface.

Figure 7 indicates the relation between the first-shedding condition (the dotted line) and the current spin period (the dashed line). To compare the first shedding with structural failure, we also plot the upper bound of structural failure of the whole volume (discussed later) at friction angles of 0° , 45° , and 90° by solid lines. If the spin state is below these lines,

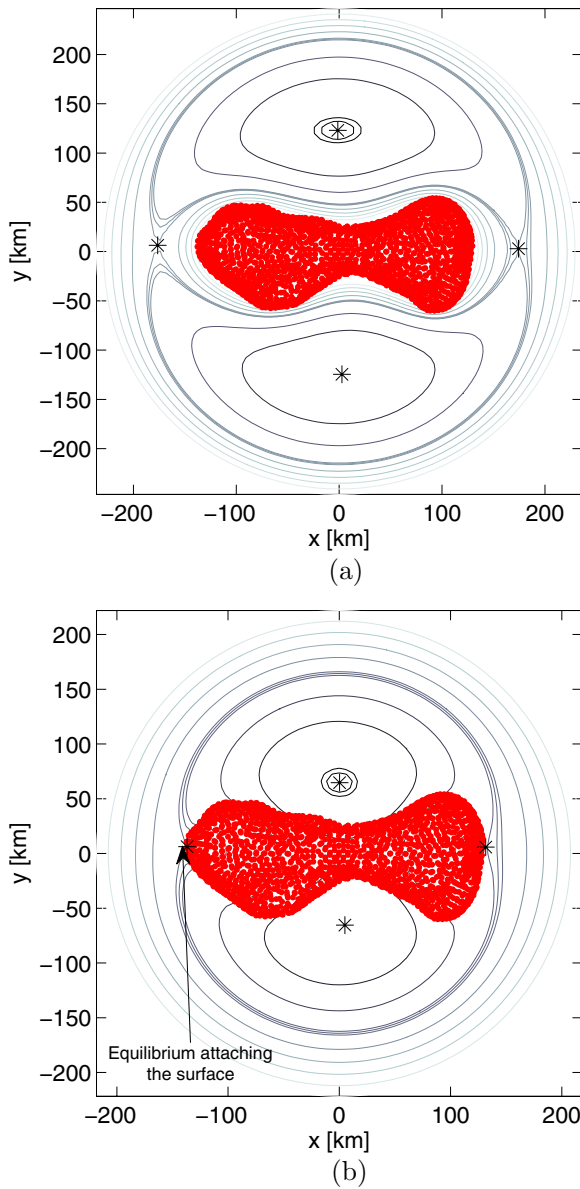


Figure 6. Zero-velocity curves for a size scale of 1.22, i.e., the Descamps et al. (2011) size. (a) shows the curves for the current spin period, i.e., 5.385 hr, and (b) describes those for a spin period of 2.81 hr at which the equilibrium point on the left reaches the surface.

(A color version of this figure is available in the online journal.)

the body must experience structural failure. It is found that the first-shedding condition occurs with a much faster spin period than structural failure. Also, the current spin period is not faster than the first-shedding condition in the test scale range.

It is worth noting that although the first shedding is obtained numerically, the force balance between the gravitational and the centrifugal force, i.e., $r_{\text{Ostro}}\alpha\Omega_{cr}^2 \propto GM/(r_{\text{Ostro}}\alpha)^2$, gives an analytical trend as

$$T_{cr} \propto \alpha^{3/2}, \quad (12)$$

where r_{Ostro} is the distance between the origin of the primary and the surface of the Ostro et al. (2000) size, M is the mass of the primary, α is the size scale, Ω_{cr} is the first shedding, and $T_{cr} = 2\pi/\Omega_{cr}$.

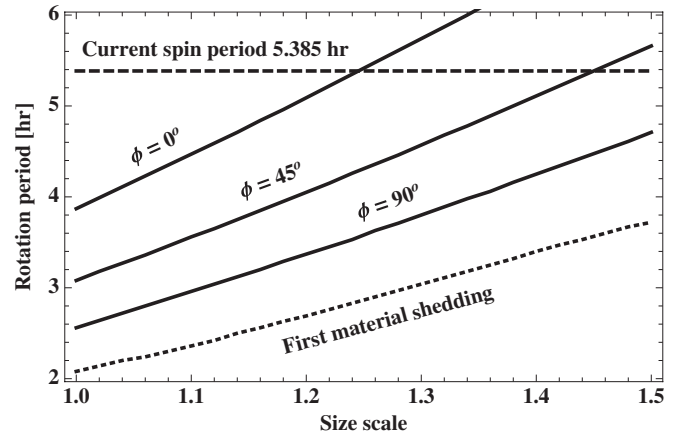


Figure 7. First shedding (the dotted line) and the yield condition by the total-volume stresses (the solid lines) as a function of the size scale. ϕ is the angle of friction. The first shedding is always below structural failure.

5.1.2. Hypothesis of Satellites' Origin

As stated by Descamps et al. (2011), the satellites are considered byproducts of a spin-up process leading to material shedding. Here, we use the technique for determining the first shedding; however, since we have already seen the zero-velocity curves of this asteroid earlier, we only track the location of the equilibrium points. The physical properties of these satellites are given in Table 2. Also, it is assumed that their orbital planes are parallel to the equatorial plane of (216) Kleopatra, as given by Descamps et al. (2011).

The satellites are supposed to be small uniformed spheres. We call these satellites the test bodies. Initially, the test bodies are supposed to be located at the edges along the minor principal axis. The initial spin period is given by conservation of the total angular momentum. Here, we neglect any other mass ejections' processes in the past for this consideration. On the assumption of zero eccentricity, the initial spin rate of the primary ω_0 can be written as

$$\omega_0 = \frac{I_z \omega_c + m_1 R_1 \Omega_1^2 + m_2 R_2 \Omega_2^2}{I_z + (m_1 + m_2) r_{\text{Ostro}}^2 \alpha^2}, \quad (13)$$

where m_i and R_i ($i = 1, 2$) are the mass and the current distance from the center of mass of the primary, respectively; I_z is the moment of inertia of the z axis of the primary; and ω_c is the current spin rate. Substitutions of the physical values in Table 2 into this equation determines the initial spin period as 5.086 hr.

In this model, if the lifting condition satisfies, it is possible for the test bodies to initiate the satellites' formation. Technically, this condition is equivalent to the condition where the saddle points are closer to the surface than the center of mass of the test bodies at this spin period. However, in this analysis, to make a stronger condition, we define that the test bodies lift off when the distance between the saddle points and the surface is less than the sum of these bodies' diameters, i.e., 15.8 km. Figure 8 shows the distance of the saddle points from the surface, d_{eqm} (the solid lines), and a distance of 15.8 km (the dashed line). Since, as shown earlier, surface shedding may occur on the left and right sides at almost the same rotation period, we track the distances of both points. The saddle point on the left side is always closer to the surface. The result shows that in the test scale range, the distances of the saddle points on both sides from the surface are never shorter than 15.8 km, and the test

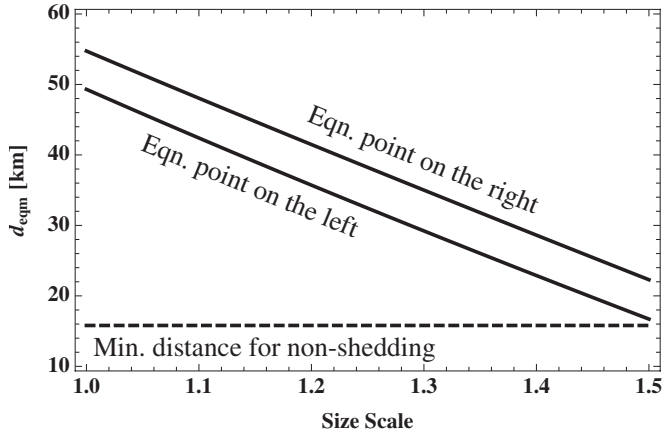


Figure 8. Relation between the distance of the equilibrium points from the surface (the solid lines) and the minimal distance where material shedding does not occur, i.e., 15.8 km (the dashed line). This plot shows the case of a spin period of 5.086 hr. The period is obtained by Equation (13). The necessary condition for material shedding to originate the satellites is that the equilibrium point on the left goes below the minimal distance.

bodies cannot lift off the surface. It implies that the satellites do not result from simple fission of the original system but may involve other processes such as the re-accumulation of an impact-generated debris disk.

5.2. Structural Failure as a Function of Size

First, we discuss the lower bound. Since elastic solutions are independent of Young's modulus, we set the modulus as 10 GPa, which may be larger than usual geological materials on the Earth. On the other hand, different Poisson's ratios provide different solutions; therefore, we investigate two cases: Poisson's ratio = 0.2 and 0.333. In the experiments, we investigate elastic solutions of 25 different size scales in the test scale range, i.e., $\alpha = 1.00, 1.02, 1.04, \dots, 1.50$. The result shows that in all the size scales, the solution includes elastic states which violate the MC condition even when $\phi = 90^\circ$. It implies that (216) Kleopatra has plastic deformation of some small elements somewhere in all the test scale ranges. Again, this does not mean that it experiences plastic failure.

Figures 9–11 show the elastic solutions which exceed $\phi = 50^\circ$ (the stars) and those which cannot be in the elastic region even when $\phi = 90^\circ$ (the circles). The dots indicate the shape of (216) Kleopatra. In addition, these figures describe the cases $\alpha = 1.00, \alpha = 1.30$, and $\alpha = 1.50$, respectively. Each case is shown by the two Poisson's ratios: (1) 0.2 and (2) 0.333. It is found that in all the cases, although different Poisson's ratios give different solutions, the results are not significantly different. In Figure 9, there are the stars around the surface of the neck, while the circles are scattered on the whole surface. In Figure 10, the stars appear around the surface of the neck, but on the opposite side of $\alpha = 1.00$. On the other hand, as shown in Figure 11, the case $\alpha = 1.50$ indicates that the stars and the circles are condensed around the neck. From this analysis, it is found that (216) Kleopatra is always above the lower bound of structural failure in the test scale range.

The upper-bound condition of the partial volume is calculated by the following: The most sensitive cross section to structural failure is evaluated by using \bar{T}_{11}^a . Figure 12 shows the stress component in the vertical axis and a scaled length normalized by the equivalent radius in the horizontal axis. The body size

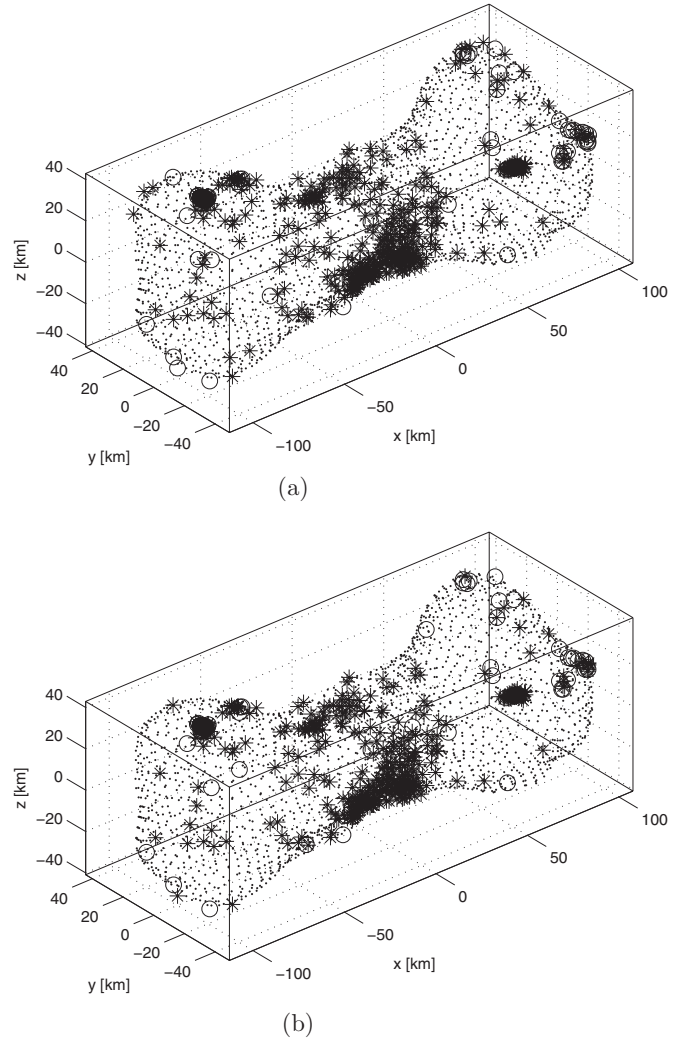


Figure 9. Elastic solutions for $\alpha = 1.00$. The stars describes the stress states at which the friction angle exceeds 50° . The circles mean that the stress states cannot be in the elastic region, even when the friction angle is 90° . The dots describe the shape of (216) Kleopatra. (a) indicates the solution for Poisson's ratio = 0.2, while (b) shows the solution for Poisson's ratio = 0.333. It is found that different Poisson's ratios give different results, but they have similar features. The stars mainly appear around the surface of the neck, while the circles are scattered on the whole surface.

along the minor principal axis ranges from -2.1 to 1.9 . Later, any lengths are introduced by the normalized length. When $\alpha = 1.00$, since the body density is large, the body force is dominated by the self-gravity. As the size scale increases, however, the magnitude of the centrifugal force increases, and there appears a stress peak in the middle. At $\alpha = 1.30$, the peak reaches the zero-tension, and the tension region starts spreading over the body. This result implies that the neck part located in the middle is quite sensitive to structural failure. In the following, to focus on the neck, we define the partial volume by the cuts at -0.21 and 0.58 .

Since (216) Kleopatra is considered a cohesionless body, only the angle of friction is a free parameter. Here, we obtain the friction angle using the upper-bound techniques. This friction angle is identical to the minimal friction angle at which the body can keep the original shape. More precisely, if the actual friction angle of the total (partial) volume is lower than the minimal friction angle, the total (partial) volume should fail.

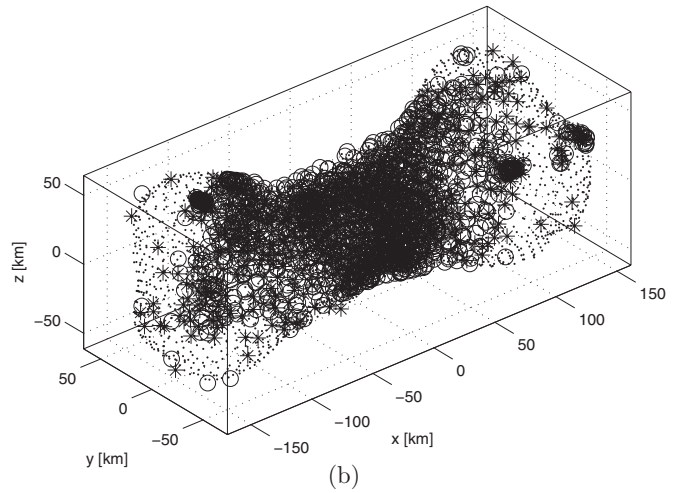
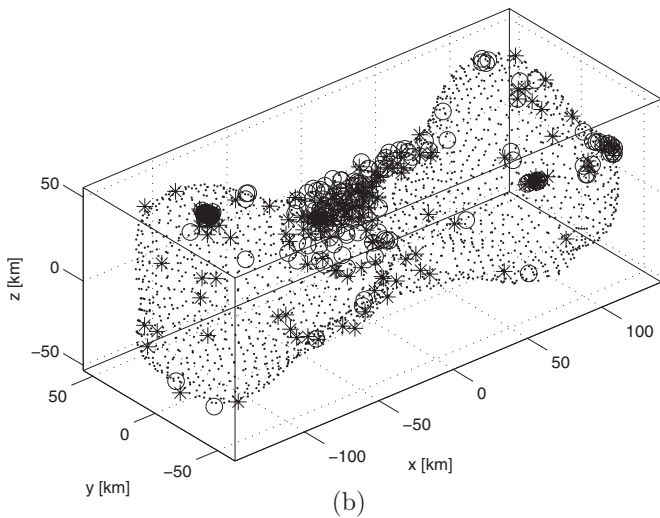
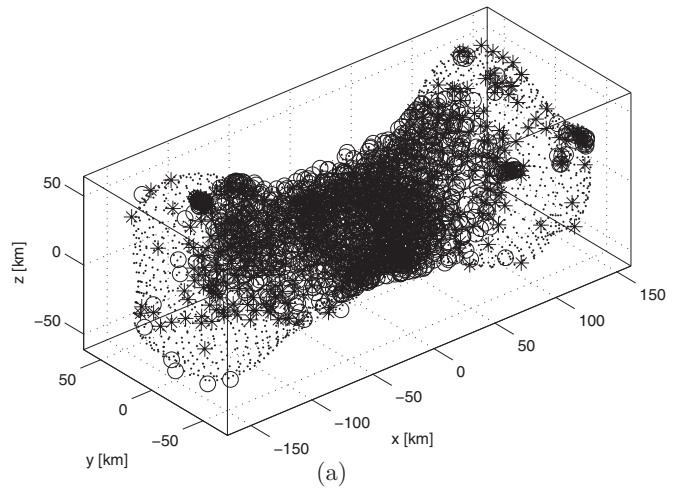
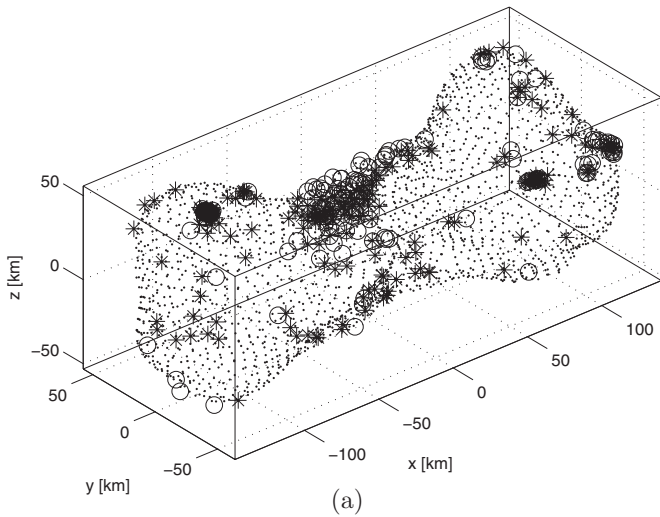
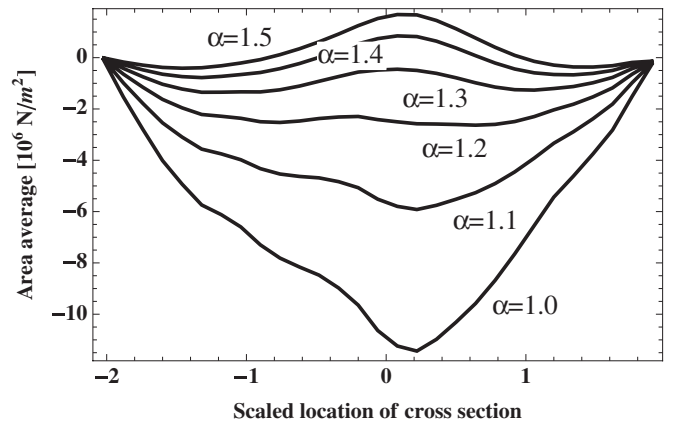


Figure 10. Elastic solutions for $\alpha = 1.30$. We use the definitions given in Figure 9. The stars assemble on the surface of the neck; however, in contrast to $\alpha = 1.00$, their locations are on the opposite side of the neck. The circles also appear near the stars.

Figure 11. Elastic solutions for $\alpha = 1.50$. Again, we use the definitions given in Figure 9. In this case, the stars and circles spread out over the whole neck.

Since the most sensitive part is chosen as the partial volume, the actual friction angle should be always above the minimal friction angle of the partial volume. Figure 13 shows the minimal friction angles of the total volume and that of the partial volume as functions of the size scale α . The minimal friction angle of the total volume keeps small angles in small scales and increases gradually. Also, when the size scale is 1.24, there is the minimal value $\sim 1^\circ$. On the other hand, the minimal friction angle of the partial volume is relatively high in a small scale, $\sim 43^\circ$ at $\alpha = 1.0$, but small around the middle, $\sim 14^\circ$ at $\alpha = 1.28$. Then, when the size scale is larger than 1.28, this friction angle increases dramatically. Since the minimal friction angle of the partial volume is always larger than that of the total volume, it can be concluded that the neck part is more sensitive to structural failure than the whole body.



6. DISCUSSION

Before the discussion, we introduce a possible friction angle of (216) Kleopatra. Scott (1963) showed that friction angles depend on a materials' porosity (see Figures 7–5(a)–(c) on

Figure 12. Minor-axis component of the averaged normal stresses as a function of locations of the normal cross sections. The negative value is compression, while the positive value is tension. Note that using the normalized length, we adjust the locations of the cross section so that the bodies with different size scales match their edges equally. The normalized length is given by dividing the location by the equivalent radius. When $\alpha = 1.3$, the part around the neck starts experiencing zero tension, which is the most sensitive to structural failure.

p. 309). On the other hand, according to Ostro et al. (2000), (216) Kleopatra's surface properties are comparable to lunar soil. They also stated that the estimated bulk density, 3.5 g cm^{-3} , is consistent with either a solid enstatite-chondritic surface or

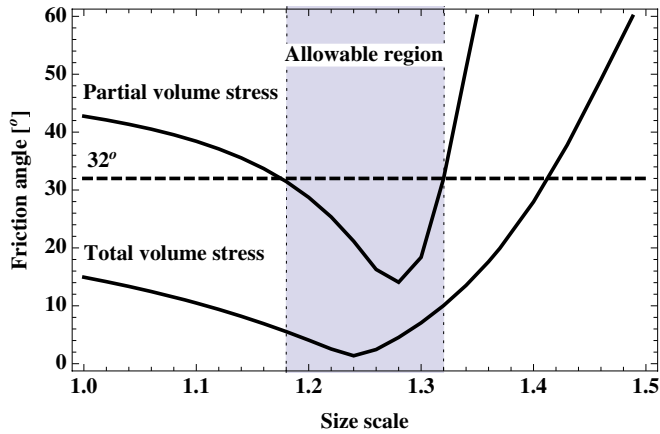


Figure 13. Minimal friction angles of the total-volume stress and partial-volume stress (the solid lines) and the assumed Kleopatra’s friction angle of 32° (the dashed line). The shaded region where the actual friction angle is larger than the minimal friction angle associated with the partial-volume stress is allowable for the existence of the current shape.

(A color version of this figure is available in the online journal.)

a metallic surface with porosity of $<60\%$.⁷ We assume this asteroid’s porosity as 44% , the mean value for lunar soil (which ranges from 33% to 55%). Figures 7–5(a) on p. 309 by Scott (1963) shows that at a porosity of 44% , an allowable friction angle is 32° . We suppose that the body has a uniform structure as well. From these facts and assumptions, in the following discussion, the friction angle of (216) Kleopatra is fixed at 32° . This implies that the body fails when the minimal friction angle is greater than 32° .

Interestingly, Figure 13 reveals that the allowable size scale lies between 1.18 and 1.32. This fact implies that if the size scale is not in this range, (216) Kleopatra cannot hold the current neck part. At a friction angle of 15° , the lowest minimal friction angle of the partial volume, where the size scale is 1.15, this asteroid encounters the most relaxed configuration. However, it does not mean that this asteroid’s stress should be at this point. The important point here is that only the range between 1.18 and 1.32 is structurally allowable. Since the bulk density is from 2.9 to 3.8 g cm^{-3} , our estimation is consistent with Ostro et al.’s (2000) surface density estimation and with Descamps et al.’s (2011) bulk density estimation. From this result, the nominal size estimated by Ostro et al. (2000) is somewhat small, while that by Marchis et al. (2012) is relatively large. On the other hand, the estimation by Descamps et al. (2011) corresponds to our size evaluation. Note that their error estimations include our result. If the size is assumed to be the Descamps et al. (2011) size, the minimal friction angle is no less than 27° , which is within the usual friction angles of geological materials (from 30° to 45°).

(216) Kleopatra may be sitting near plastic structural failure at the current spin period because the stable region for the current shape, especially the neck, is relatively small. Pravec et al. (2007) showed the spin barrier as a function of light curve amplitude (which is a proxy for asteroid equatorial elongation). Especially, in Figure 2 in their paper, the theoretical curves defined for ellipsoidal figures and for a friction angle of 90° indicate that the barrier shifts to lower spin rates for complex shapes and lower friction angles. Our result is consistent with

their interpretation. Therefore, the neck may play an important role in sustaining the whole body; this asteroid may not be a contact binary composed of two bodies that loosely rest on each other. It means that this part might have been stretched plastically to get the current shape. It can be imagined that the narrow neck part is the byproduct of plastic deformation, and the original shape should have a wider neck and be less elongated than the current shape. We emphasize anew that neither a Yarkovsky-O’Keefe-Radzievskii-Paddack (YORP) effect nor tidal perturbation have a significant effect on the spin-state change of this asteroid.

In contrast to plastic failure, material shedding cannot occur at the current spin period. As shown in Figure 7, material shedding does not happen even if this asteroid spins up to the condition where a material with a friction angle of 90° encounters structural failure of the whole body. In addition, Figure 8 shows that the distance between the surface and the equilibrium points does not reach the size of these satellites in the test scale range.

7. CONCLUSION

This paper explored the dynamical and structural stability of the shape of Asteroid (216) Kleopatra at the current spin period, varying the shape size. We separately investigated the material shedding condition and the structural failure condition. To find the condition where material shedding occurs first, we constructed the zero-velocity surfaces to find the dynamical equilibrium points and the constraints of the motion. The result shows that (216) Kleopatra cannot experience material shedding at the current spin period, and the satellites orbiting about the primary do not result from the shedding process. On other hand, to determine the lower and upper bounds of structural failure, we utilized limit analysis. It is found that the body, especially the neck part, is very sensitive to structural failure. Using elastic solutions, we revealed that (216) Kleopatra is always above the lower bound in the test scale range. Referring to Scott (1963) to determine the friction angle of (216) Kleopatra as 32° , we found that only the size scale between 1.18 and 1.32 allows the body to be structurally stable. Our study agreed with the Descamps et al. (2011) size estimation.

The authors thank Dr. Keith A. Holsapple for his dedicated technical advice. The authors are also grateful to Dr. Pascal Descamps for the information about the estimation for the orbits of the satellites, Dr. Petr Pravec for useful discussion about the spin barrier for large elongated asteroids, Dr. Mikko Kaasalainen for useful discussion about their model of Kleopatra, and Dr. Frank Marchis for useful discussion about their estimation techniques.

APPENDIX

COMPARISON OF THE EQUILIBRIUM POINTS BETWEEN YU & BAOYIN (2012, 2013) AND OUR COMPUTATION

We show a comparison between Yu & Baoyin (2012, 2013) and our computation in Table 3. Note that we recalculate their results of the equilibrium points by using our code, so these values are slightly different from those by Yu & Baoyin (2012, 2013). This difference results from computational thresholds in our code. As mentioned in the main text, we assume that the mass is fixed at $4.64 \times 10^{18} \text{ kg}$. If we choose the Ostro et al.

⁷ As discussed earlier, given the Descamps et al. (2011) mass, the Ostro et al. (2000) density may be more than 6.0 g cm^{-3} .

Table 3
Comparison of the Equilibrium Points by Yu & Baoyin (2012, 2013)
and Our Computations

Property	Yu & Baoyin (2012, 2013)	Our Computation
Volume (km ³)	7.09×10^5	7.09×10^5
Density (g cm ⁻³)	3.6	6.5
Mass (kg)	2.55×10^{18}	4.64×10^{18}
Equilibrium (km)		
E_1	$x 1.43 \times 10^2$	1.66×10^2
	$y 2.44$	2.27
	$z 1.18$	7.91×10^{-1}
E_2	$x -1.45 \times 10^2$	-1.67×10^2
	$y 5.19$	4.97
	$z -2.72 \times 10^{-1}$	-5.47×10^{-2}
E_3	$x 2.22$	1.26
	$y -1.02 \times 10^2$	-1.31×10^2
	$z -2.72 \times 10^{-1}$	1.71×10^{-1}
E_4	$x -1.17$	-1.59
	$y 1.01 \times 10^2$	1.30×10^2
	$z -5.46 \times 10^{-1}$	-3.32×10^{-1}

Notes. Notations E_i ($i = 1, \dots, 4$) are based on Table 1 in Yu & Baoyin (2012). Note that we recalculate their results by using our code, but they are slightly different from their values in Table 1 in Yu & Baoyin (2012). This arises from the convergent thresholds defined in our code.

(2000) size, the density should be ~ 6.5 g cm⁻³. Therefore, the equilibrium points from our code are farther away from the surface than those from Yu & Baoyin (2012, 2013).

REFERENCES

- Bus, S. J., & Binzel, R. P. 2002, *Icar*, **158**, 146
- Cellino, A., Pannunzio, R., Zappala, V., Farinella, P., & Paolicchi, P. 1985, *A&A*, **144**, 355
- Chakrabarty, J. 2006, *Theory of Plasticity* (3rd ed.; Oxford: Butterworth-Heinemann)
- Chen, W. F., & Han, D. J. 1988, *Plasticity for Structural Engineers* (New York: Springer)
- Chree, C. 1889, *QJPAM*, **27**, 338
- Chree, C. 1891, *The London, Edinburgh, and Dublin Philosophical Magazine and Journal of Science*, **32**, 233
- Davidsson, B. J. R. 2001, *Icar*, **149**, 375
- Descamps, P., Marchis, F., Berthier, J., et al. 2011, *Icar*, **211**, 1022
- Dobrovolskis, A. R. 1982, *Icar*, **52**, 136
- Dunham, D. W., Osborn, W., Williams, G., et al. 1991, in *Int. Conf. Asteroids Comets, Meteors* (Houston, TX: Lunar and Planetary Institute), 54
- Eriguchi, Y., Hachisu, I., & Sugimoto, D. 1982, *PThPh*, **67**, 1068
- Guibout, V., & Scheeres, D. J. 2003, *CeMDA*, **87**, 263
- Hestroffer, D., Berthier, J., Descamps, P., et al. 2002a, *A&A*, **392**, 729
- Hestroffer, D., Marchis, F., Fusco, T., & Berthier, J. 2002b, *A&A*, **394**, 339
- Holsapple, K. A. 2004, *Icar*, **172**, 272
- Holsapple, K. A. 2007, *Icar*, **187**, 500
- Holsapple, K. A. 2008, *IJNLM*, **43**, 733
- Holsapple, K. A. 2010, *Icar*, **205**, 430
- Holsapple, K. A. 2001, *Icar*, **154**, 432
- Kaasalainen, M., & Viikinkoski, M. 2012, *A&A*, **543**, A97
- Kadish, J., Barber, J., Washabaugh, P. D., & Scheeres, D. J. 2008, *Solids Struct.*, **45**, 540
- Love, A. E. H. 1944, *A Treatise on the Mathematical Theory of Elasticity* (Cambridge: Cambridge Univ. Press)
- Magnusson, P. 1990, *Icar*, **85**, 229
- Marchis, F., Enriquez, J., Emery, J., et al. 2012, *Icar*, **221**, 1130
- Mitchell, D. L., Ostro, S. J., & Rosema, K. D. 1995, *Icar*, **118**, 105
- Ostro, S. J., Hudson, R. S., Nolan, M. C., et al. 2000, *Sci*, **288**, 836
- Ostro, S. J., Margot, J.-L., Benner, L. A. M., et al. 2006, *Sci*, **314**, 1276
- Pravec, P., Harris, A. W., & Warner, B. D. 2007, in *IAU Symp., Near Earth Objects, Our Celestial Neighbors: Opportunity and Risk*, ed. A. Milani, G. B. Valsecchi, & D. Vokrouhlický (Cambridge: Cambridge Univ. Press), 167
- Sanchez, P., & Scheeres, D. J. 2012, *Icar*, **218**, 876
- Scaltriti, F., & Zappala, V. 1978, *Icar*, **34**, 428
- Scott, R. F. 1963, *Principles of Soil Mechanics* (Boston, MA: Addison-Wesley)
- Sharma, I. 2009, *Icar*, **200**, 636
- Sharma, I. 2010, *Icar*, **205**, 638
- Takahashi, S., Shinokawa, K., Yoshida, F., et al. 2004, *EP&S*, **56**, 997
- Tanga, P., Hestroffer, D., Berthier, J., et al. 2001, *Icar*, **153**, 451
- Tedesco, E. F., Noah, P. V., Noah, M., & and, S. D. P. 2002, *AJ*, **123**, 1056
- Tholen, D. J. 1984, PhD thesis, Univ. Arizona
- Walsh, K. J., Richardson, D. C., & Michel, P. 2008, *Natur*, **454**, 188
- Walsh, K. J., Richardson, D. C., & Michel, P. 2012, *Icar*, **220**, 514
- Washabaugh, P. D., & Scheeres, D. J. 2002, *Icar*, **159**, 314
- Weidenschilling, S. J. 1980, *Icar*, **44**, 807
- Werner, R. A., & Scheeres, D. J. 1997, *CeMDA*, **65**, 313
- Yu, Y., & Baoyin, H. 2012, *AJ*, **143**, 62
- Yu, Y., & Baoyin, H. 2013, *Ap&SS*, **343**, 74
- Zappala, V., Martino, M. D., & Scaltriti, F. 1983, *Icar*, **53**, 458